THE JOURNAL OF PHYSICAL CHEMISTRY A
A JOURNAL OF THE AMERICAN CHEMICAL SOCIETY

pubs.acs.org/JPCA Article

Spray-Flame Synthesis of $LaFe_xCo_{1-x}O_3$ ($x = 0.2, 0.3$) Perovskite Nanoparticles for Oxygen Evolution Reaction in Water Splitting: Effect of Precursor Chemistry (Acetates and Nitrates)

Published as part of The Journal of Physical Chemistry virtual special issue "Combustion in a Sustainable World: From Molecules to Processes".

Steven Angel,* Michael Braun, Baris Alkan, Joachim Landers, Soma Salamon, Heiko Wende, Corina Andronescu, Christof Schulz, and Hartmut Wiggers

Cite This: J. Phys. Chem. A 2023, 127, 2564−2576 Read Online

ACCESS | Metrics & More | Article Recommendations | Supporting Information

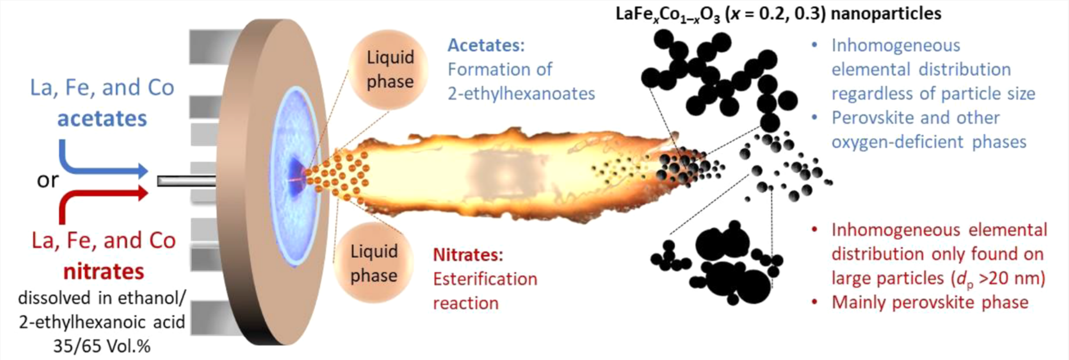

ABSTRACT: The product properties of mixed oxide nanoparticles generated via spray-flame synthesis depend on an intricate interplay of solvent and precursor chemistries in the processed solution. The effect of two different sets of metal precursors, acetates and nitrates, dissolved in a mixture of ethanol (35 Vol.%) and 2-ethylhexanoic acid (2-EHA, 65 Vol.%) was investigated for the synthesis of $LaFe_xCo_{1-x}O_3$ ($x = 0.2, 0.3$) perovskites. Regardless of the set of precursors, similar particle-size distributions ($d_p = 8$−11 nm) were obtained and a few particles with sizes above 20 nm were identified with transmission electron microscopy (TEM) measurements. Using acetates as precursors, inhomogeneous La, Fe, and Co elemental distributions were obtained for all particle sizes according to energy dispersive X-ray (EDX) mappings, connected to the formation of multiple secondary phases such as oxygen-deficient $La_3(Fe_xCo_{1-x})_3O_8$ brownmillerite or $La_4(Fe_xCo_{1-x})_3O_{10}$ Ruddlesden−Popper (RP) structures besides the main trigonal perovskite phase. For samples synthesized from nitrates, inhomogeneous elemental distributions were observed for large particles only where La and Fe enrichment occurred in combination with the formation of a secondary $La_2(Fe_xCo_{1-x})O_4$ RP phase. Such variations can be attributed to reactions in the solution prior to injection in the flame as well as precursor-dependent variations in in-flame reactions. Therefore, the precursor solutions were analyzed by temperature-dependent attenuated total reflection Fourier-transform infrared (ATR-FTIR) measurements. The acetate-based precursor solutions indicated the partial conversion of, mainly La and Fe, acetates to metal 2-ethylhexanoates. In the nitrate-based solutions, esterification of ethanol and 2-EHA played the most important role. The synthesized nanoparticle samples were characterized by BET (Brunauer, Emmett, Teller), FTIR, Mössbauer, and X-ray photoelectron spectroscopy (XPS). All samples were tested as oxygen evolution reaction (OER) catalysts, and similar electrocatalytic activities were recorded when evaluating the potential required to reach 10 mA/cm^2 current density (∼1.61 V vs reversible hydrogen electrode (RHE)).

1. INTRODUCTION

Hydrogen is envisioned to play a pivotal role in the decarbonization of the global economy as a strategy to mitigate the emission of greenhouse gases and related climate change effects.[1] Since 2017, many of the world's strongest economies introduced hydrogen initiatives[1] that involve the

Received: September 15, 2022
Revised: March 1, 2023
Published: March 10, 2023

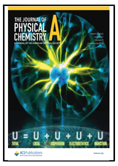

https://doi.org/10.1021/acs.jpca.2c06601
J. Phys. Chem. A 2023, 127, 2564−2576

sustainable generation of hydrogen from electrochemical water splitting (e.g., alkaline water electrolysis).

Electrochemical water splitting requires active catalyst materials that enable the evolution of H_2 and O_2 at high rates. From both reactions, the main bottleneck is the anodic oxygen evolution reaction (OER) that has been associated with sluggish kinetics caused by the transfer of four protons coupled to four electrons, requiring potentials higher than the theoretical value of 1.23 V at pH = 0.[2,3] In recent years, several classes of materials (e.g., noble metal oxides, perovskite oxides, spinel oxides, sulfides, hydroxides, selenides) have been investigated and proposed as potential active catalysts for OER.[2] When considering a balance of aspects such as catalytic activity, durability, cost, and sustainability, perovskite oxides stand out as promising OER catalysts for alkaline elctrolysis.[4] Perovskite-based materials (ABO_3) incorporating lanthanides (A site) and 3d transition metal ions (B site) have been identified as such promising alternatives as their electronic structure and surface defects can be tuned by substituting/doping the A and B sites.[5] The $LaFe_xCo_{1-x}O_3$ perovskite is an interesting material system in which synergistic effects of the Fe/Co substitution on the OER performance have been already identified for $x = 0.3-1$.[6,7] However, challenges related to the synthesis of phase-pure cobalt-rich ($x < 0.3$) $LaFe_xCo_{1-x}O_3$ structures by conventional methods (e.g., coprecipitation synthesis) have limited the understanding of the OER activity of these Co-rich perovskite structures. Additionally, for conventional synthesis methods (e.g., mechanochemistry, sol−gel), the production of perovskites with high specific surface areas (SSAs) has proven to be challenging. This is due to the several processing steps required, typically involving high-temperature calcination, which is required to reach a phase-purity target at the expense of specific surface area. In contrast, perovskites with both high phase purity and large SSA have been successfully obtained via spray-flame synthesis (SFS).[8,9] However, this milestone has not been a simple task, since obtaining high-quality materials from spray-flame synthesis requires the selection of the right metal precursors in combination with the right solvents, as not only the nanoparticle formation processes but also the chemistry and decomposition of the precursor solutions play crucial roles.

$LaCoO_3$ and $LaFeO_3$ perovskites, with SSAs higher than 85 m^2/g, were successfully spray-flame-synthesized using metal nitrates as precursors and mixtures of ethanol (EtOH) and 2-ethylhexanoic acid (2-EHA) as solvents.[8] Here, it was shown that the EtOH/2-EHA mixtures, previously identified as a way to generate droplet microexplosions and unimodal particle-size distributions,[10,11] can be efficiently used to limit the hydrolysis of metal nitrates, especially in the case of iron nitrate. Such hydrolysis processes lead to the early formation of metal hydroxides in the solution (i.e., in droplets), which might cause the formation of large particles from the so-called droplet-to-particle mechanism.[8] This process can be especially relevant in large droplets coming from unusual time−temperature profiles as a result of flame pulsations, as it has been previously identified.[12] It was identified that the reaction of EtOH and 2-EHA can lead to the formation of ethyl 2-ethylhexanoate and water, which then promotes the further formation of hydroxides. It was proposed and later shown[13] that transition metal nitrates catalyze this esterification, especially in iron nitrate-containing solutions.

Acetates have been investigated as precursors for the spray-flame synthesis of $LaFe_xCo_{1-x}O_3$ ($x = 0-0.6$) perovskites, using 1-propanol/propionic acid/DI water[9] or 1-propanol/octanoic acid/DI water[14] mixtures as solvents. Besides in the main perovskite phase, oxygen-deficient brownmillerite and lanthanum-rich Ruddlesden−Popper phases were identified in the product powder. The use of acetates led to the formation of unimodal particle-size distributions, as it has been related to the gas-to-particle mechanism in spray-flame synthesis,[15] but to inhomogeneous cation elemental distributions in the particles. The latter aspect has not been understood so far and is analyzed in this work.

Using a solvent mixture of ethanol and 2-ethylhexanoic acid, this work explores the use of two different precursor sets, acetates and nitrates, for the spray-flame synthesis of $LaFe_xCo_{1-x}O_3$ ($x = 0.2, 0.3$) perovskite materials. The iron concentrations (x) of 0.2 and 0.3 were selected as the conventional synthesis of such perovskite structures has been challenging in the past.[7] The morphological, crystallographic, and surface properties of the synthesized materials were analyzed and compared using transmission electron microscopy (TEM)/energy dispersive X-ray (EDX), BET (Brunauer, Emmett, Teller), XRD, Fourier-transform infrared (FTIR), Mössbauer spectroscopy, and X-ray photoelectron spectroscopy (XPS) measurements. Furthermore, the precursor solutions used for the synthesis of the materials were analyzed via temperature-dependent FTIR measurements, allowing one to correlate the chemical reactions in the precursor solutions with the final materials' characteristics. All synthesized materials were evaluated as OER electrocatalysts using rotating-disk electrode (RDE) measurements.

2. METHODS

2.1. Spray-Flame Synthesis. $LaFe_xCo_{1-x}O_3$ ($x = 0.2, 0.3$) perovskite materials were spray-flame synthesized using the in-house-developed SpraySyn reactor that has been previously described.[16−18] Using a total metal-ion concentration [La + Fe + Co] of 0.2 mol/L, metal acetates[$La(CH_3CO_2)_3 \cdot xH_2O$ (99.9%, Sigma-Aldrich), $Fe(CH_3CO_2)_2$ (95%, Sigma-Aldrich), $Co(CH_3CO_2)_2 \cdot 4H_2O$ (ACS reagent, ≥98%, Sigma-Aldrich)] or metal nitrates [$La(NO_3)_3 \cdot xH_2O$ (99.9%, Sigma-Aldrich), $Fe(NO_3)_3 \cdot 9H_2O$ (ACS reagent, ≥98%, Sigma-Aldrich), $Co(NO_3)_2 \cdot 6H_2O$ (ACS reagent, ≥98%, Sigma-Aldrich)] were dissolved in a mixture of 35 Vol.% ethanol and 65 Vol.% 2-EHA to prepare the precursor solutions with a ratio of iron and cobalt that mirrors the desired elemental composition of the product. For spray formation, each solution was supplied to the burner using a syringe pump (2 mL/min) and put in close contact with a continuous flow of oxygen (6 slm, standard liters per minute) using an external-mixing atomizing nozzle, which is positioned at the center of a porous sintered bronze plate. The combustion of the spray was supported by a flat premixed methane/oxygen pilot-flame (3 slm CH_4/5 slm O_2) stabilized on the surface of the bronze plate. The pilot flame was shielded by a surrounding flow of sheath-gas (compressed air, 140 slm). The pressure in the reactor chamber was maintained in the 960−980 mbar abs. range. Downstream of the reactor zone, a quenching gas flow of compressed air (230 slm) was supplied to control the temperature of the particles and off-gases. At the end of each synthesis, the corresponding sample was collected using a membrane filter. After the synthesis, all samples were heat-treated at 300 °C for 1 h under air flow at atmospheric pressure using a Nabertherm L 1/12/

R6 muffle furnace to remove adsorbates from the surface of the materials and to prepare the nanoparticle powder for the electrochemical tests.

2.2. Characterization of the Materials. X-ray diffraction patterns were recorded in a PANalytical X′Pert PRO device operated with Cu Kα radiation (0.15406 nm, 40 kV, 40 mA). The diffractograms were recorded at $2\theta = 10-60°$ with a step size of 0.05°. Particle size, morphology, and the elemental distribution of the cations were analyzed from the images acquired in a JEOL JEM 2200FS transmission electron microscope (TEM) equipped with energy dispersive X-ray spectroscopy (EDX mapping). The specific surface areas of the samples were generated by evaluating nitrogen adsorption (Quantachrome, Nova2000) measurements using the BET (Brunauer, Emmett, Teller) theory.

Particles and precursor solutions were studied by Fourier-transform infrared spectroscopy (FTIR) from 400 to 4000 cm^{-1} using a Bruker Vertex 80 device (attenuated total reflection (ATR) sample holder, KBr beam splitter, DigiTect DLaTGS detector). X-ray photoelectron spectroscopy (XPS) measurements were carried out in a ULVAC-PHI Versaprobe II (Chanhassen, USA) with Mg Kα ($h\nu = 1253.6$ eV) as an X-ray source and a pass energy of 11.75 eV. The C 1s adventitious carbon C−C binding energy at 284.8 eV was used to calibrate the recorded spectra, analyzed by CasaXPS software. Thermogravimetric analysis (TGA) measurements were performed using a Netzsch 449 F1 Jupiter device at a temperature range between 35 and 800 °C with a heating rate of 7.5 K/min under the flow of synthetic air (250 mL/min).

For Mössbauer spectroscopy, ca. 20 mg of sample powder material was mixed with ca. 250 mg of boron nitride (BN) and pressed into a cylindrical disk of 13 mm in diameter and roughly 1 mm in thickness. Spectra were recorded at room temperature (293 K) in transmission geometry. A ^{57}Co(Rh) radiation source, mounted on a constant-acceleration driving unit, was utilized while data evaluation was performed via the "Pi" program package.

2.3. Characterization of the Solutions of Precursors. To analyze for potential nonreversible chemical transitions in the solutions of precursors, the metal acetates [$La(CH_3CO_2)_3\cdot xH_2O$ (99.9%, Sigma-Aldrich), $Fe(CH_3CO_2)_2$ (95%, Sigma-Aldrich), $Co(CH_3CO_2)_2\cdot 4H_2O$ (ACS reagent, ≥98%, Sigma-Aldrich)] or the metal nitrates [$La(NO_3)_3\cdot xH_2O$ (99.9%, Sigma-Aldrich), $Fe(NO_3)_3\cdot 9H_2O$ (ACS reagent, ≥98%, Sigma-Aldrich), $Co(NO_3)_2\cdot 6H_2O$ (ACS reagent, ≥98%, Sigma-Aldrich)] were dissolved in a mixture of ethanol (35 Vol.%) and 2-EHA (65 Vol.%) in the required molar ratios (e.g., La:0.2Fe:0.8Co, La:0.3Fe:0.7Co). Each solution was heated in a temperature-controlled oil bath from room temperature (23 °C) up to 70 °C. FTIR measurements of the solutions at both temperatures (23 and 70 °C) were conducted as previously described. Before the measurement, an aliquot of each solution was extracted with a micropipette and placed on the ATR holder of the FTIR device.

2.4. Electrochemical Measurements. Electrochemical measurements were performed in a three-electrode cell using an Autolab PGSTAT bipotentiostat/galvanostat (Metrohm) using a catalyst-coated electrode, a platinum mesh, and an Ag/AgCl (3 mol/L KCl) electrode as working, counter, and reference electrodes, respectively. The counter electrode was positioned in a compartment separated from the bulk electrolyte by a glass frit. A 1 mol/L KOH solution was purified over Chelex 100 and used as electrolyte. Catalyst inks (5 mg/mL) were prepared by dispersing each synthesized sample in a volumetric mixture (49/49/2) of ultrapure water/ethanol/Nafion solution (~5 Wt.% of Nafion in water and lower aliphatic alcohols, ~0.9 g/cm^3) to obtain a Nafion/Catalyst ratio (N/C) of 0.186 on the electrode surface. After 15 min of sonication, the corresponding ink was used to form the catalyst film by drop-casting it on a polished glassy carbon (GC) electrode.

2.4.1. Rotating Disk Electrode Experiments. In the RDE measurements, a catalyst mass loading of 210 $\mu g/cm^2$ was used. Several steps and techniques were used during the electrochemical characterization. Initially, an electrochemical impedance spectrum was collected at open-circuit potential using a frequency ranging from 50 kHz to 10 Hz using a 10 mV AC (RMS) amplitude to determine the uncompensated resistance (R_U). After, a conditioning step was conducted by performing ten cyclic voltammograms in a potential window of −0.040 to 0.410 V vs Ag/AgCl (3 mol/L KCl) with a scan rate of 100 mV/s without rotation. Following the conditioning step, a linear sweep voltammetry (LSV) was recorded in the potential window from 0.0 to 0.8 V vs Ag/AgCl (3 mol/L KCl) with a scan rate of 5 mV/s at a rotation speed of 1600 rpm, and this was used to evaluate and compare the electrocatalytic activity of all materials. All measured potentials were converted to the reversible hydrogen electrode (RHE) scale and corrected for the *iR*-drop according to eq 1.

$$E_{RHE} = E_{Ag/AgCl/3mol/l\,KCl} + 0.207 + 0.059pH - IR_U \quad (1)$$

where E_{RHE} is the potential of the working electrode referenced to the RHE scale, $E_{Ag/ACl/3\ mol/L\ KCl}$ is the measured potential of the working electrode referenced to 3 mol/L KCl, 0.207 is the value corresponding to the formal potential of the Ag/AgCl (3 mol/L KCl) reference electrode, I is the current, and R_u is the uncompensated resistance.

3. RESULTS AND DISCUSSION

3.1. Characterization of Spray-Flame Synthesized $LaFe_xCo_{1-x}O_3$ (x = 0.2, 0.3) Nanoparticles Using Acetates or Nitrates as Precursors. Solutions containing either organic (La-, Fe-, Co-acetate) or inorganic (La-, Fe-, Co-nitrate) metal precursor salts dissolved in ethanol (35 Vol.%) and 2-EHA (65 Vol.%) were used for the spray-flame synthesis of $LaFe_xCo_{1-x}O_3$ (x = 0.2, 0.3) nanoparticles, as described in Section 2.1. After synthesis, all samples were heat-treated at 300 °C for 1 h under air flow at atmospheric pressure to remove adsorbates originating from the synthesis process. The removal of adsorbed species (e.g., carboxylates) was evidenced with FTIR measurements of the as-synthesized and heat-treated samples presented in Figure S9. Additionally, thermogravimetric analysis (TGA) measurements of the as-synthesized samples (Figure S10) indicate that >95 Wt.% of the adsorbates are removed when the samples are heated at 300 °C. The heat-treatment process did not affect the phase composition/concentration or the crystallite sizes of the samples as it can be seen in the Rietveld refinements presented in Figures S5 to S8 and Tables S1 and S2. Consequently, only the heat-treated samples, which were characterized by TEM, XRD, EDX, XPS, and Mössbauer spectroscopy, were analyzed and compared in the manuscript.

Particle-size distributions (i.e., histograms fitted to log-normal size distributions) obtained from the analysis of TEM images are presented in Figure 1 for the acetate- and the

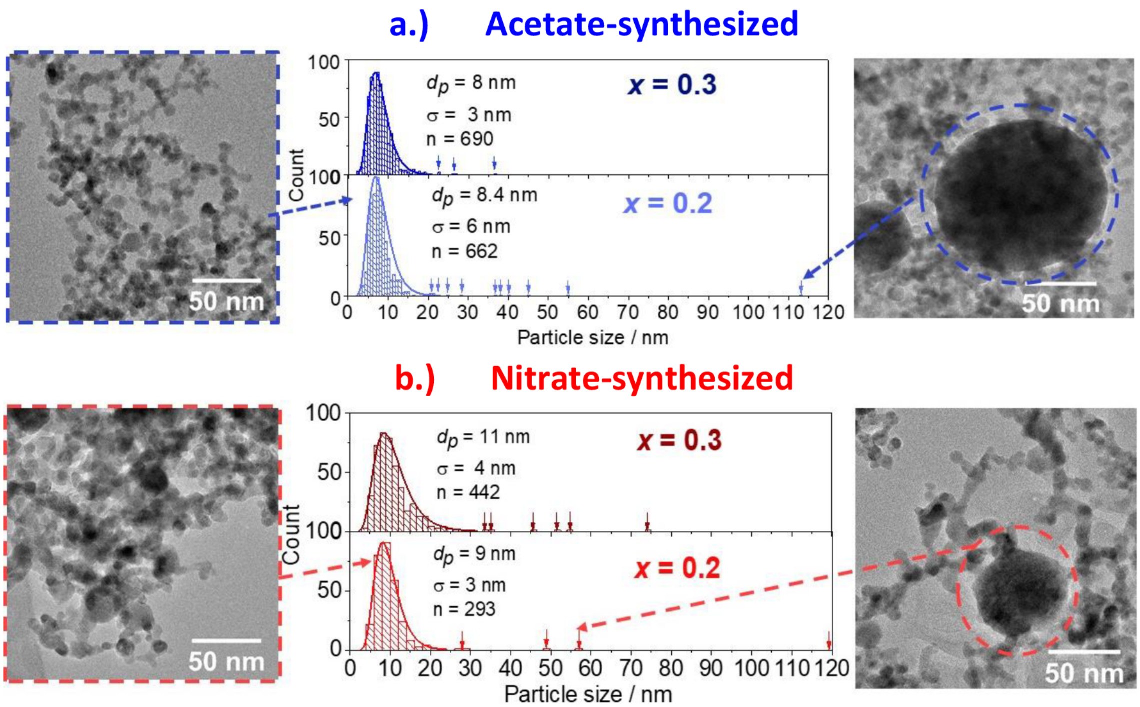

Figure 1. TEM particle-size distributions of $LaFe_xCo_{1-x}O_3$ (x = 0.2, 0.3) samples spray-flame synthesized using (a) acetate or (b) nitrate precursors. TEM images of a region of small particles are presented on the left and identified large particles, on the right.

nitrate-based samples. The two acetate-based samples exhibited a similar average particle size (d_p^{TEM}) of 8 nm as presented in Figure 1a. An example of these small particles is presented on the left TEM picture in Figure 1a. In the histograms, identified large particles (>20 nm), which are out of the log-normal distributions, are indicated with arrows, and an example of a 113 nm particle from the x = 0.2 sample is presented on the right TEM image from Figure 1a. It is important to mention that the x = 0.2 sample does not necessarily have a higher number of large particles than the x = 0.3 sample; a statistically representative account of these particles cannot be obtained solely from the obtained TEM images.

Compared to the samples synthesized from acetates, nitrate-based samples (Figure 1b) show a slightly larger average particle size (d_p^{TEM}) of 9 and 11 nm for x = 0.2 and 0.3, respectively. An example of these small particles (<20 nm) is presented on the left of Figure 1b. Large particles were also identified and indicated with arrows in the figure. A 57 nm particle is presented on the right TEM image from Figure 1b.

Even though similar particle-size distributions (up to 20 nm) were obtained for all samples (Figure 1), BET-specific surface areas of the x = 0.3 samples deviated from those of the x = 0.2 samples produced from both acetate and nitrate precursors (Figure 2).

Regardless of the metal precursor type, the x = 0.2 samples present a similar BET SSA (~100 m^2/g). Samples with a higher iron concentration (x = 0.3) present lower BET SSAs, 61 and 88 m^2/g for the nitrate- and acetate-based samples, respectively (Figure 2). Assuming monodisperse and spherical particles, the BET-derived particle sizes (d_p^{BET}) were calculated to be ~8.5 nm for both nitrate- and acetate-based x = 0.2 samples, ~14 nm for the nitrate-based x = 0.3 sample, and ~9.5 nm for the acetate-based x = 0.3 sample. The d_p^{BET} values of the x = 0.2 samples closely match the values (d_p^{TEM}) obtained from the TEM particle-size distributions (Figure 1), indicating a low content of large particles in both samples. This is not the case for the x = 0.3 samples in which the d_p^{BET} values, when compared with the d_p^{TEM} values, indicate a higher content of the large particles, especially for the nitrate-based sample.

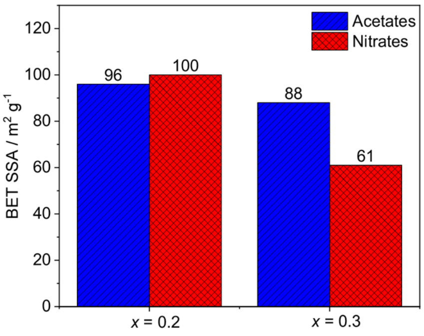

Figure 2. BET-specific surface areas (SSA) of $LaFe_xCo_{1-x}O_3$ (x = 0.2, 0.3) samples spray-flame synthesized using acetates or nitrates as metal precursors.

The phase composition of the samples was analyzed by X-ray diffraction (XRD), and the corresponding patterns are presented in Figure 3. The region between 30° and 35° was amplified in the diffractograms to better present the qualitative phase analysis. For all cases and regardless of the precursor type, the trigonal $LaFe_xCo_{1-x}O_3$ perovskite phase with space group $R\bar{3}cH$ was indexed (ICSD 190099: $LaFe_{0.2}Co_{0.8}O_3$). This phase shows two high-intensity reflections at ~32.9° and ~33.2° that are more clearly separated in the diffractograms from the nitrate-based samples (inset in Figure 3b). Furthermore, when increasing the content of iron from 20% to 30%, the diffractogram shifted to lower θ values, indicating the expansion of the unit cell as the ionic radius of Fe^{3+} (0.645

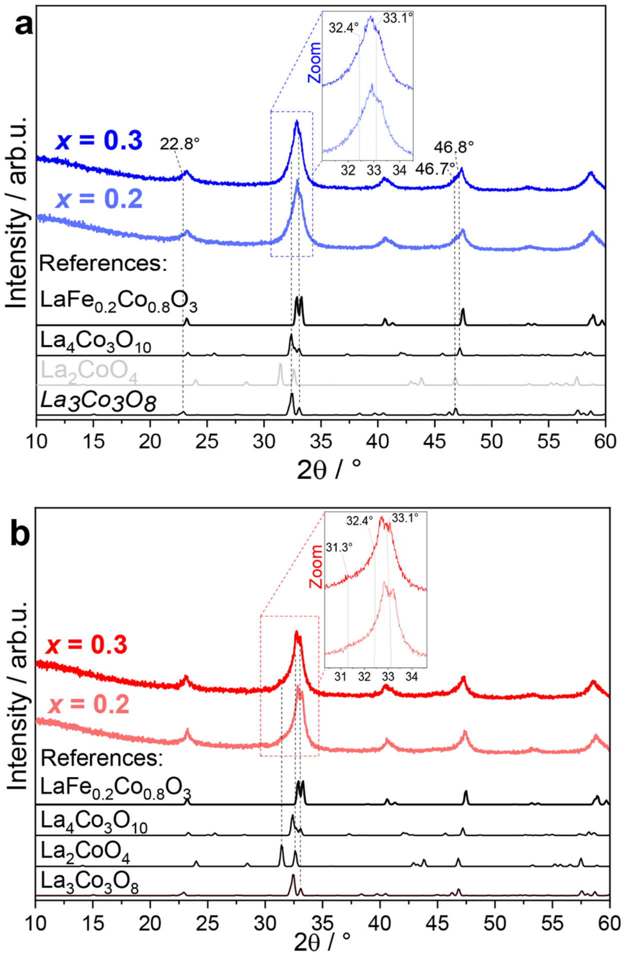

Figure 3. XRD patterns of $LaFe_xCo_{1-x}O_3$ (x = 0.2, 0.3) samples spray-flame synthesized using (a) acetates or (b) nitrates as precursors.

Å) is higher than that of Co^{3+} (0.610 Å)[19] and the Fe−O bond energy is lower than that of Co−O in the perovskite structure.[20] This shift was not observed in the acetate-based sample containing 30% Fe (Figure 3a).

Besides the main peaks of the stoichiometric perovskite phase, additional features were identified in all diffractograms. For the acetate-based materials (Figure 3a), the shoulders at ~46.8° and ~22.8° indicate that two substructures are present in low concentration: (1) the monoclinic $La_3(Fe_xCo_{1-x})_3O_8$ brownmillerite phase with space group $P1211$ (ICSD 51198: $La_3Co_3O_8$ or $LaCoO_{2.67}$), which is an oxygen-deficient perovskite-related structure missing one-ninth of the oxygen atoms, and (2) the monoclinic $La_4(Fe_xCo_{1-x})_3O_{10}$ Ruddlesden−Popper (RP) perovskite-type phase with space group $C12/m1$ (ICSD 51177: $La_4Co_3O_{10}$). Depending on the cobalt oxidation state and the amount of iron, this phase can develop a deficiency or excess of oxygen. The main reflections (~32.4° and ~33.1°) of these two secondary phases overlap with the main reflections (~32.9° and ~33.2°) of the rhombohedral perovskite structure. Comparable results are also found in the nitrate-based materials. The reflections at ~32.4° and ~33.1° presented in the inset of Figure 3b hint at the presence of the $La_4Co_3O_{10}$ and/or $La_3Co_3O_8$ secondary phases in low concentrations, especially in the x = 0.3 case. Additionally, another substructure was identified (Figure 3b): the tetragonal $La_2(Fe_xCo_{1-x})O_4$ Ruddlesden−Popper (RP) phase with space group $I4/mmm$ (ICSD 16404: La_2CoO_4), whose main peak is located at ~31.3°.

The presence of lanthanum-rich structures (e.g., $La_4Co_3O_{10}$ or La_2CoO_4) indicates the possibility of counting with lanthanum-deficient perovskite-related structures and/or isolated cobalt and/or iron oxides. Even though single oxides were not identified in the XRD patterns (Figure 3), the presence of such structures cannot be ruled out, as they might be present in the samples in low concentrations and as small particles. Regarding the lanthanum-deficient structures, the decrease of lanthanum in the perovskite-related structures

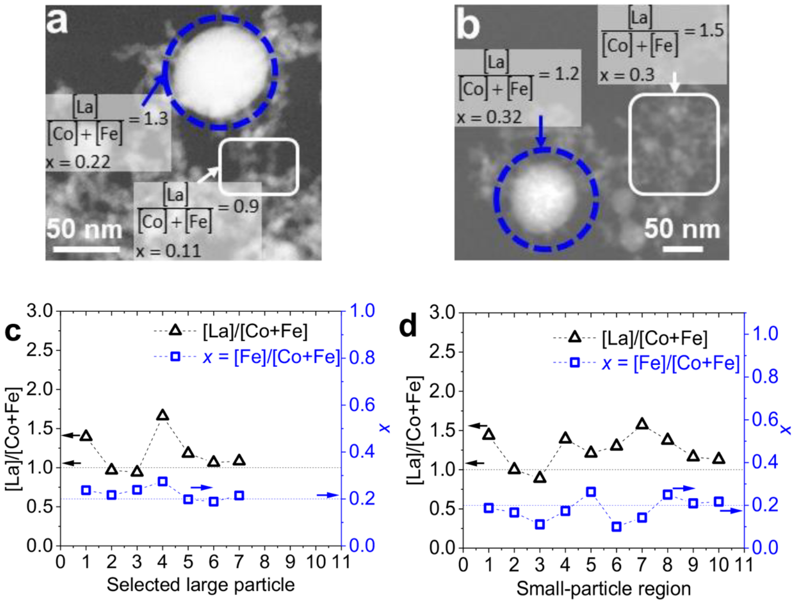

Figure 4. TEM images of the acetate-based (a) x = 0.2 and (b) x = 0.3 $LaFe_xCo_{1-x}O_3$ samples. [La]/[Co + Fe] and x = [Fe]/[Co + Fe] ratios calculated from EDX measurements of (c) selected large particles (d_p > 20 nm) and (d) regions of small particles of the acetate-based x = 0.2 sample.

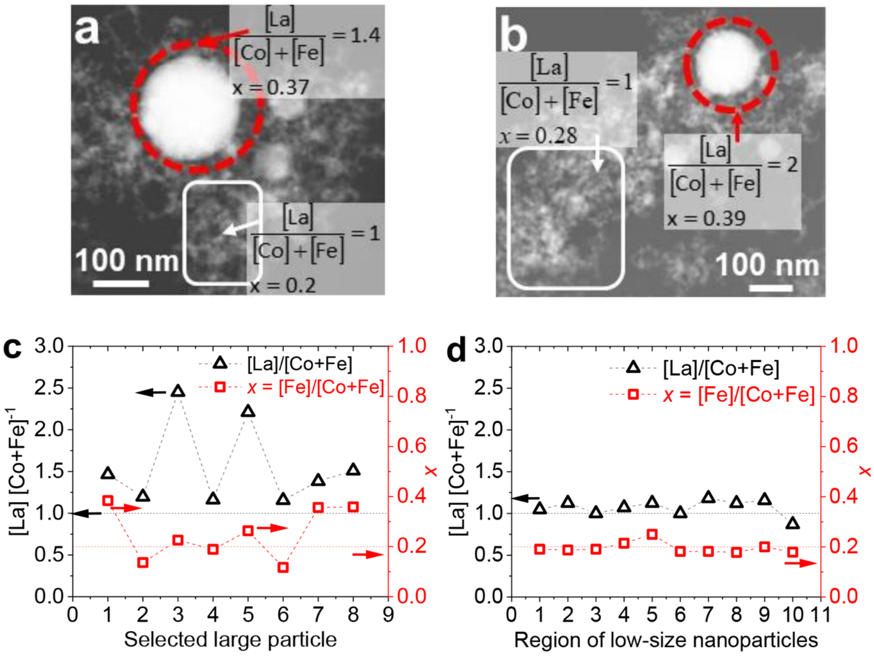

Figure 5. TEM images of the nitrate-based (a) $x = 0.2$ and (b) $x = 0.3$ $LaFe_xCo_{1-x}O_3$ samples. [La]/[Co + Fe] and x = [Fe]/[Co + Fe] ratios calculated from EDX measurements of (c) selected large particles ($d_p > 20$ nm) and (d) regions of small particles of the nitrate-based $x = 0.2$ sample.

would also generate a decrease of the unit cell volume of the structure(s), causing the shift of the XRD peaks to higher 2θ values as it has been observed for $La_{0.9}CoO_3$ and for La_wCoO_3 (w = 0.7, 0.8, 0.9, 1, 1.1) perovskites.[21,22] As mentioned above, the acetate-based samples did not show peak-shifting (Figure 3a), an effect that might not be due to a lack of proper iron doping but to an averaging effect of high-unit-cell-volume La-stoichiometric/La-rich structures and low-unit-cell-volume lanthanum-deficient structures. This is underlined by the fact that the XRD signals are less sharp as in the case of the nitrate-based materials. To verify the presence of such La-rich/La-deficient structures and to analyze the atomic distribution of iron and cobalt in the different samples, energy-dispersive X-ray spectra (EDX) were taken from selected areas and particles and the atomic ratios of lanthanum to the sum of the transition metal ions ([La]/[Co + Fe]) were calculated along with the atomic fraction of iron in relation to the total content of iron and cobalt (x = [Fe]/[Co + Fe]). For the acetate-based samples, TEM images with EDX results are presented in Figure 4 for the $x = 0.2$ and $= 0.3$ samples. The lanthanum-to-transition metal ratio and the atomic ratio of iron are presented for the $x = 0.2$ sample analyzing two cases, identified large particles ($d_p > 20$ nm) (Figure 4c) and selected regions of small particles (Figure 4d).

The acetate-based $x = 0.2$ sample presented single large particles with lanthanum-to-transition metal ratios ([La]/[Co + Fe]) from 1 to 1.6 and iron ratios with respect to the total Fe and Co amount (x = [Fe]/[Co + Fe]) ranging from 0.2 to 0.26 (Figure 4c). A 56 nm particle is presented in Figure 4a with a lanthanum-to-transition metal ratio of 1.3 and an iron ratio (x) of 0.22. This indicates La and Fe enrichment in the large particles. The enrichment was also identified in regions consisting of small (<20 nm) nanoparticles (Figure 4d) with lanthanum-to-transition metal ratios up to 1.5 (average of 1.3 as in the $La_4(Fe_xCo_{1-x})_3O_{10}$ RP phase) and iron ratios (x) up to 0.25. Nevertheless, these regions presented mainly low ratios of iron (x), in the range from 0.10 to 0.20, with lanthanum-to-transition metal ratios as low as 0.9 as presented as well in Figure 4a and as expected based on the XRD analysis from Figure 3a. As references, inductively coupled plasma mass spectrometry (ICP-MS) measurements of the acetate- and nitrate-based $x = 0.2$ samples, presented in Table S3, indicate that the samples have practically the same global elemental composition. Regarding the acetate-based $x = 0.3$ sample (Figure 4b), large particles, as well as regions containing small particles, show an enrichment of lanthanum (lanthanum-to-transition metal ratios up to 1.5) and a slightly higher iron amount than what is stoichiometrically expected. In the acetate-based samples, the Fe and La enrichment is not an exclusive feature of large particles, since this can also be observed in the regions containing small nanoparticles. Nevertheless, low concentrations of lanthanum and especially of iron were more frequently found in the regions of small particles.

Regarding the nitrate-based samples, the $x = 0.2$ sample presented lanthanum-to-transition metal ratios ranging between 1.1 and 2.5 and iron ratios (x) between 0.11 and 0.37 in the large particles as it can be observed in Figure 5a,c. In contrast, the measurements in regions of small nanoparticles presented a homogeneous elemental distribution, with lanthanum-to-transition metal ratios of ∼1 (or slightly lower, ∼0.9 in some regions) and iron ratios (x) of ∼0.18. Similarly, as presented in Figure 5b, the $x = 0.3$ sample contains La- and Fe-rich large particles, while the regions of small nanoparticles have homogeneous lanthanum-to-transition metal ratios of ∼1 or ∼0.9 in some regions and iron ratios of ∼0.28, to compensate the enrichment in the large particles. Compared with the acetate-based samples in which the lanthanum-to-transition metal ratios and the iron ratios are highly variable in both large- and small-particle regions, the nitrate-based samples show a strong enrichment of La and high variability of the Fe concentration only in the large particles. Considering that the acetate- and nitrate-based $x = 0.2$ samples have similar particle-size distributions (Figure 1) and BET-specific surface areas (Figure 2) and based on the XRD patterns from Figure 3 as well as on the EDX results (Figures 4 and 5), it is identified that the acetate-based sample has a higher La, Co, and Fe elemental disorder than the nitrate-based sample, represented in the presence of a variety of phases (most likely oxygen-deficient phases according to the XRD results from Figure 3) deviating from the stoichiometric perovskite structure. As the structural differences in the acetate- and nitrate-based samples might create differences in the local environment and coordination of the transition metal ions with oxygen, Mössbauer spectra were recorded at room temperature (RT, 293 K) (Figure 6) and measured for all samples to analyze the oxidation state and coordination of iron ions and the magnetic environment of the samples.

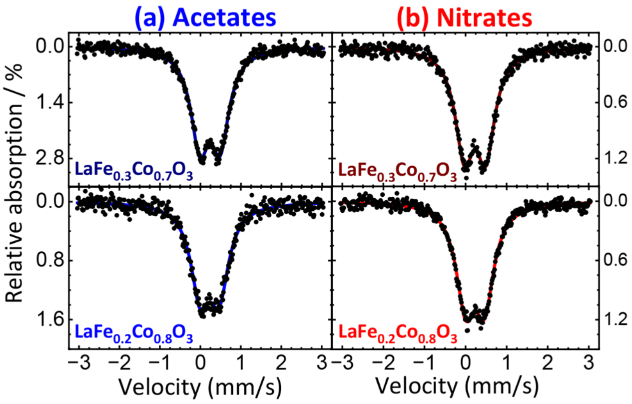

Figure 6. Room temperature Mössbauer spectra of (a) acetate- and (b) nitrate-based spray-flame synthesized $LaFe_xCo_{1-x}O_3$ ($x = 0.2, 0.3$) samples.

As it can be observed in the Mössbauer data obtained at room temperature (RT) (Figure 6), all samples display doublet spectra with isomer shifts close to 0.34 mm/s relative to α-Fe, usually indicative of Fe^{3+} with a high-spin (HS: $S = 5/2$) configuration.[23] The doublets exhibit a quadrupole splitting of ca. 0.47 mm/s for $x = 0.2$ and 0.51 mm/s for $x = 0.3$. The spectra show no clear evidence of further subspectra; contributions from low fractions of Fe^{3+}-bearing byphases of similar spectral structure identified in XRD may be superimposed by the main doublet. They would thereby only result in very minor variations in the extracted hyperfine parameters of the perovskite phase, as discussed further in the following in regard to Fe coordination and structural information from XRD analysis.

FeO_5 oxygen-defect configurations (trigonal/square bipyramidal coordination with RT isomer shifts typically between ~0.2 and ~0.3 mm/s)[24] as found in the Mo-substituted $Sr_3Fe_2O_{7-\delta}$ most likely occur in the identified $La_4(Fe_xCo_{1-x})_3O_{10}$ Ruddlesden−Popper (RP) phase,[25] especially in the acetate-based samples. On the other hand, FeO_4 oxygen-defect configurations (tetrahedral coordination with RT isomer shifts typically between ~0.1 and ~0.3 mm/s)[24] most likely happen in brownmillerite-type structures (e.g., the identified $La_3(Fe_xCo_{1-x})_3O_8$ phase), in which tetrahedral oxygen-deficient BO_4 (B: transition metal ion) layers alternate with octahedral BO_6 layers.[26] The FeO_6 configurations (for perovskite-type structures at room temperature with isomer shifts usually ranging between ≈0.3 and ≈0.4 mm/s)[24] correspond to structures without oxygen vacancies as in the identified $LaFe_xCo_{1-x}O_3$ perovskite phase in both acetate- and nitrate-based samples.[27,28]

As indicated above, the Mössbauer results suggest the presence of iron with a predominant oxidation state of 3+ (Fe^{3+}) in the different analyzed samples and regardless of the metal-precursor type. This observation is supported by the Fe 2p XPS spectra results presented in Figure S1, in which Fe^{3+} is also identified as the main oxidation state of the surface iron ions.[19] Thus, the precursor type does not seem to affect the oxidation state of iron. Similarly, the oxidation state of cobalt was not affected by the use of acetate- or nitrate-based metal precursors as presented in the Co 2p XPS spectra (Figure S2).[29−31] Nevertheless, the Co oxidation state was affected by the iron content of the prepared materials. The $x = 0.2$ samples (acetate- and nitrate-based) show a Co^{3+}/Co^{2+} ratio of 2, while the $x = 0.3$ samples have a higher Co^{2+} content ($Co^{3+}/Co^{2+} = 1.2$). Contrary to the Fe and Co results, the C 1s XPS spectra (Figure S3) of the acetate-based samples present clear variations with respect to the nitrate-based samples. The acetate-based samples exhibit a higher relative content of C═O/O−C−O surface species[32,33] as indicated by the peak at binding energies (B.E.) of ≈288.5 eV, while the nitrate-based samples show a higher relative content of surface metal carbonates (B.E. ≈ 289 eV).[34,35] Congruently, the La 3d XPS spectra (Figure S4) of the nitrate-based samples present, besides the characteristic La $3d_{5/2}$ multiplet splitting of perovskite-like structures (4.2 eV)[36] also found in the acetate-based samples, an additional La $3d_{5/2}$ multiplet splitting of 3.6 eV related to lanthanum carbonate species.[35] In order to further investigate the catalysts, ATR-FTIR spectra of the samples were recorded and are presented in Figure 7a.

Infrared bands at 843, 1050, 1367, and 1480 cm^{-1} were assigned to the characteristic π, $\nu(C{-}O_I) + \nu(C{-}O_{II})$, $\nu(C{-}O_{II}) + \nu(C{-}O_I)$, and $\nu(C{-}O_{II})$ vibrations of unidentate carbonates (Figure 7a), respectively.[37] These bands are more intense and, hence, point to a higher content of unidentate carbonates in the nitrate-based samples than in the acetate-based ones as similarly identified with the XPS results. The formation of unidentate carbonates on the surface of La_2O_3 or $LaCoO_3$ materials[38,39] has been related to the adsorption of CO_2 on medium strength Lewis basic sites as O^{2-} anions which are bonded to metal ions.[40] Compared to the nitrate-based samples, the lower content of carbonates in the acetate-based samples might be related to the presence of a higher concentration of oxygen (O^{2-})-deficient phases as identified with the XRD analysis (Figure 3), also related to a possible lower iron−oxygen coordination as indicated in the Mössbauer spectroscopy data analysis (Figure 6). Besides the metal carbonate bands, asymmetric (ν_{as}, 1636 cm^{-1}) and symmetric (ν_s, 1346 cm^{-1}) carboxylate (COO) bands were also identified in all materials (Figure 7).[41,42] An approximation to the possible coordination mode of the carboxylate groups can be done based on the separation of the carboxylate bands ($\nu_{as} - \nu_s$).[43] In this case, a separation of 290 cm^{-1} indicates a metal-carboxylate unidentate coordination mode.

A detail of the FTIR spectra between 400 and 750 cm^{-1} is presented in Figure 7b. The infrared bands in this region are related to M−O (M: transition metal ions) vibrations in the perovskite-like structures. Two strong infrared bands were identified at 536 and 600 cm^{-1}, which have been related to low-spin (LS) and higher spin (e.g., intermediate-spin (IS) or

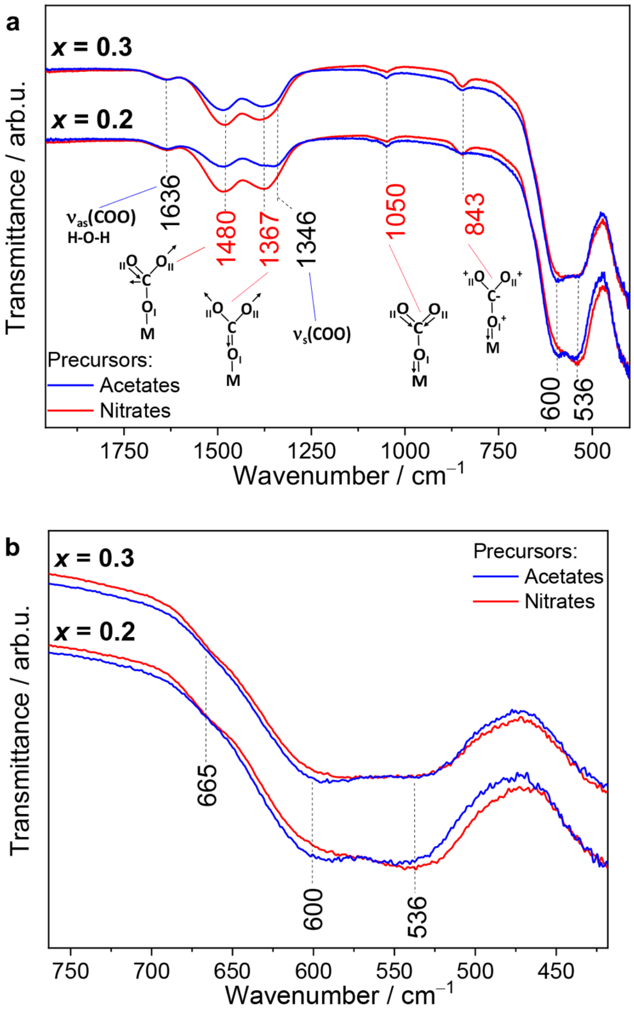

Figure 7. (a) ATR-FTIR spectra of acetate- and nitrate-based $LaFe_xCo_{1-x}O_3$ (x = 0.2, 0.3) samples with (b) an amplified region between 800 and 400 cm^{-1}.

high-spin (HS)) states of cobalt ions, respectively.[44,45] The acetate-based samples present a slightly higher relative intensity of the IS state band than the nitrate-based samples as it can be observed in Figure 7b, which can be related to the favored IS state of Co ions near oxygen (O^{2-}) vacancies,[46,47] also supporting the finding regarding a higher content of oxygen-deficient phases in the acetate-based samples.

In summary, the use of acetates or nitrates as precursors in the spray-flame synthesis of $LaFe_xCo_{1-x}O_3$ materials mainly influences the elemental distribution of La, Fe, and Co in the final particles. The acetate-based samples present a random and inhomogeneous distribution of metal ions regardless of the particle size. In contrast, the nitrate-based samples present an enrichment of La and Fe mainly in the few encountered large particles (d_p > 20 nm), while the small particles (average size of ~10 nm) contain a homogeneous elemental distribution of La, Fe, and Co. Especially in the acetate-based samples, the strong variation in elemental distribution causes the formation and stabilization of (oxygen-deficient) perovskite-like secondary phases (e.g., brownmillerite, RP phases) with a lower Fe—O/Co—O coordination than in the nitrate-based samples.

The materials' properties of the perovskite-like catalysts can be finely tuned with the selection of the metal precursor type. Still, the understanding of how the metal acetates/metal nitrates cause the mentioned variations is not clear. While the acetate group acts as a reducing agent probably influencing the formation of oxygen-deficient perovskite-like phases in the spray-flame process, the nitrate group acts as an oxidizing agent causing the contrary effect. Additionally, when compared to metal nitrates, the use of metal acetates represents an additional energy source coming from the exothermic oxidation of the acetate group, which might further increase the local flame temperatures, although this effect is probably small given the low precursor concentration. Nevertheless, the high variation in the La, Fe, and Co elemental distribution in all particles of the acetate-based samples and in the large particles of the nitrate-based samples cannot be explained with the already mentioned effects. To estimate effects that still occur in the liquid phase prior to complete droplet combustion (e.g., during heating and evaporation of droplets) on the elemental distribution in the synthesized particles, an ATR-FTIR study regarding the chemical stability of the precursor solutions was performed and is presented in the following section.

3.2. Temperature-Dependent ATR-FTIR Analysis of Precursor Solutions.

The ATR-FTIR (attenuated total reflection Fourier-transform infrared) analysis of precursor solutions was performed as explained in Section 2.3. The solutions were prepared by dissolving the corresponding precursor(s) in a mixture of ethanol (35 Vol.%) and 2-EHA (65 Vol.%) with a total precursor concentration of 0.2 mol/L. Magnetically agitated vials containing 20 mL of the prepared solutions were heated in an oil bath from room temperature until 70 °C, and at both initial and final temperatures, ATR-FTIR spectra of aliquots of the solutions were analyzed to detect possible variations in the precursors and solvents.

3.2.1. Acetates as Precursors. The recorded ATR-FTIR spectra of a solution containing $La(CH_3CO_2)_3{\cdot}H_2O$ in a mixture of 35 Vol.% ethanol and 65 Vol.% of 2-EHA are presented in Figure 8a. At 23 °C, the characteristic vibrations of the acetate ion were identified: asymmetric COO^- vibrations at 1552 and 1530 cm^{-1}, ν(C—C) at 960, 950, and 942 cm^{-1}, δ(OCO) at 667 cm^{-1}, and $\pi(COO^-)/\pi(CH)$ at 610 cm^{-1}.[48,49] Heating the solution up to 70 °C caused a significant decrease in the intensity of all acetate bands while the intensity of the band at 1589 cm^{-1} increased together with a shoulder at 1550 cm^{-1}. These bands are attributed to the formation of lanthanum(III) tris(2-ethylhexanoate),[50,51] suggesting a ligand-exchange reaction between lanthanum acetate and 2-EHA to form 2-ethylhexanoate and acetic acid. The use of acetates and long-chain carboxylic acids has been extensively investigated for the formation of metal (Cu, Ru, Mo, Rh) 2-ethylhexanoates.[52]

ATR-FTIR spectra of solutions containing iron acetate or cobalt acetate in 35 Vol.% ethanol and 65 Vol.% 2-EHA were also recorded. In the iron acetate solution case (Figure 8b), the band at 1591 cm^{-1} corresponds to the $\nu_{as}(COO^-)$ vibration of an iron carboxylate,[53] suggesting the formation of iron(II) bis(2-ethylhexanoate). The intensity of this band increased with the modification of the temperature of the solution from 23 to 70 °C, indicating a higher concentration of the carboxylate. In the cobalt acetate solution case (Figure 8c), the bands at 1613 and 1550 cm^{-1} correspond to the asymmetric COO^- vibrations[54] of a cobalt carboxylate, indicating the formation of cobalt bis(2-ethylhexanoate). Nevertheless, the intensities of the cobalt carboxylate bands

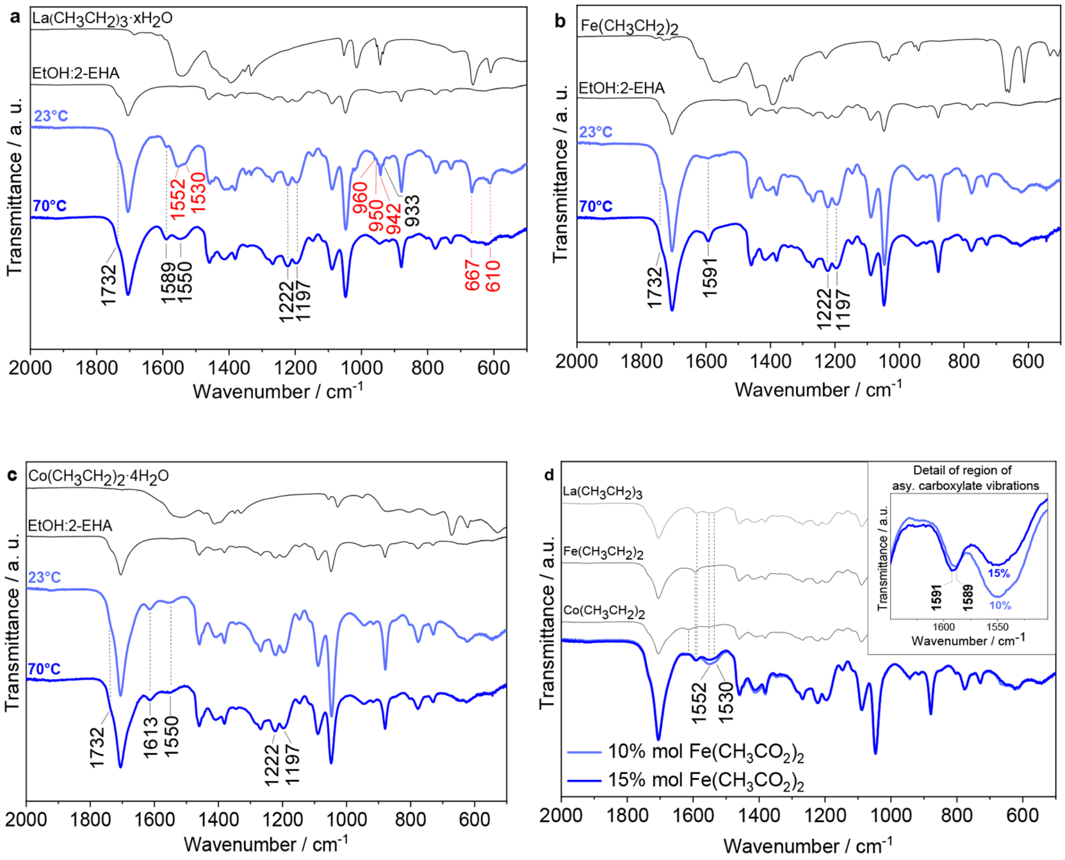

Figure 8. ATR-FTIR spectra at 23 and 70 °C of (a) lanthanum acetate, (b) iron acetate, (c) cobalt acetate, and (d) La-/Fe-/Co-acetate in a mixture of 35 Vol.% ethanol and 65 Vol.% 2-EHA.

did not increase with a higher temperature and were not as strong as those from lanthanum (Figure 8a) and iron carboxylates (Figure 8b). Besides the carboxylate vibration bands, three bands at 1732, 1222, and 1197 cm^{-1} were identified in all cases (Figure 8c), corresponding to the asymmetric C═O (1732 cm^{-1}) and symmetric C−O (1222 and 1197 cm^{-1}) ester vibrations.[55,56] This is an indication of the esterification reaction of ethanol and 2-EHA forming ethyl 2-ethylhexanoate and water.[13]

To analyze the interaction of the three metal acetates in solutions of ethanol and 2-EHA, ATR-FTIR spectra (Figure 8d) of solutions containing 10 or 15 mol % $Fe(CH_3CO_2)_2$ (corresponding to the Fe/(Fe + Co) ratio of 0.2 or 0.3), 40 or 35 mol % $Co(CH_3CO_2)_2$, and 50 mol % $La(CH_3CO_2)_3$ were recorded. The spectra presented in Figure 8d were recorded at 70 °C and are compared with the previously analyzed spectra of the single acetate solutions at 70 °C (Figure 8a−c). With a concentration of iron acetate of 10 mol %, the conversion of lanthanum acetate to lanthanum tris(2-ethylhexanoate) was slowed down as evidenced by the presence and intensity of the asymmetric COO^- vibrations at 1552 and 1530 cm^{-1}. The lanthanum carboxylate band at 1589 cm^{-1} overlaps with the iron carboxylate band at 1591 cm^{-1}, and the carboxylate band of cobalt bis(2-ethylhexanoate) at 1613 cm^{-1} was not identified. As presented in the inset from Figure 8d, increasing the concentration of iron acetate to 15 mol % caused the shifting of the asymmetric carboxylate band from 1589 to 1591 cm^{-1}, suggesting the formation of iron carboxylate, that was also verified with the decrease of the intensities of the bands at 1552 and 1530 cm^{-1}. These results hint to the preferential ligand-exchange reaction of iron acetate with 2-EHA to form iron carboxylate over the lanthanum carboxylate. Furthermore, the formation of a cobalt carboxylate was not encountered when iron acetate was present in solution.

3.2.2. Nitrates as Precursors.

ATR-FTIR spectra of solutions containing $La(NO_3)_3{\cdot}xH_2O/Fe(NO_3)_2{\cdot}9\ H_2O$ or $La(NO_3)_3{\cdot}xH_2O/Co(NO_3)_2{\cdot}6\ H_2O$ in mixtures of 35 Vol.% ethanol and 65 Vol.% 2-EHA were analyzed separately in a previous publication.[8] As background information, it was identified that the characteristic asymmetric COO^- vibrations of metal carboxylates were only present in solutions containing iron nitrate. Furthermore, it was also identified that 2-EHA is useful to limit the hydrolysis of iron and the low temperature formation of iron hydroxides. Additionally, it was proposed that iron nitrate is possibly acting as a catalyst in the esterification reaction between ethanol and 2-EHA.

For the sake of completeness and for comparison in the current study, ATR-FTIR measurements were carried out here regarding the interaction of lanthanum, iron, and cobalt nitrates in a solution of 35 Vol.% of ethanol and 65 Vol.% of 2-EHA at 70 °C. The recorded spectra are presented in Figure 9 and correspond to solutions containing 10 or 15 mol % $Fe(NO_3)_3$ (corresponding to the Fe/(Fe + Co) ratio of 0.2 or 0.3), 40 or 35 mol % $Co(NO_3)_2$, and 50 mol % $La(NO_3)_3$. As ATR-FTIR measurements of the two solutions at room and other temperatures did not present appreciable variations, they are not included in Figure 9.

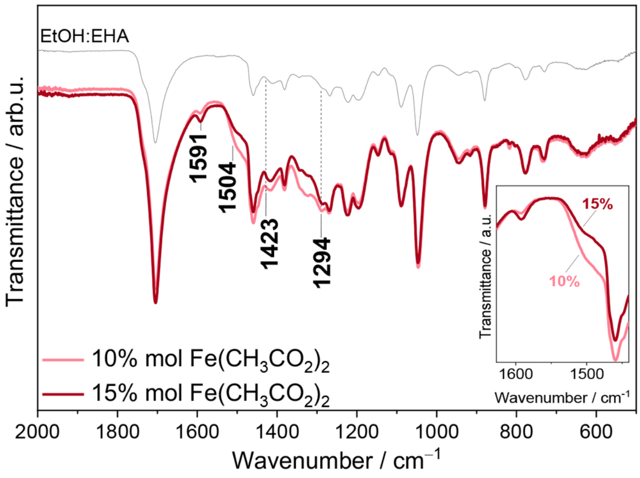

Figure 9. ATR-FTIR spectra at 23 and 70 °C of La-/Fe-/Co-nitrate in a mixture of 35 Vol.% ethanol and 65 Vol.% 2-EHA.

In the solution containing 10 mol % of iron nitrate, the vibration bands at 1504, 1423, and 1294 cm^{-1} were identified and assigned to protonated 2-EHA.[57] The protonation of the carboxylic acid has been associated with the first step of the general esterification mechanism.[58] The increase of the concentration of iron nitrate caused the decrease of the intensity of the protonated carboxylic acid and a slight increase of asymmetric[53] COO$^-$ vibration intensity at 1591 cm^{-1} as presented in the inset from Figure 9, which corresponds to a slightly higher concentration of iron 2-ethylhexanoate in solution. The low formation of iron carboxylate might be a source of the required initial protons for the catalytic esterification reaction. The formation of water derived from this reaction might also lead to the hydrolysis of iron and the subsequent formation of iron hydroxides at low temperatures.[13]

Comparing the ATR-FTIR results of the acetate-based solutions to those of the nitrate-based solutions, the formation of iron and lanthanum (only from La-acetate) carboxylates is taking place more effectively when acetates are used as metal precursors. While a low-temperature ligand-exchange reaction of cobalt acetate was not identified, the heating of the acetate-based solutions generates two different La and Fe precursors (acetates and 2-ethylhexanoates), indicating a variety of precursors in the spray droplets. The formation of these two types of precursors (acetates and 2-ethylhexanoates) most likely influences the inhomogeneous elemental distribution of the metal ions in the final particles based on different decomposition kinetics of acetate and 2-ethylhexanoate precursors. A comparison of the thermal decomposition of (La, Fe, Co) 2-ethylhexanoates with the corresponding acetate precursors cannot be directly done due to the scarcely reported data of the decomposition of (La, Fe, Co) 2-ethylhexanoates. Nevertheless, reported data of cerium acetate and cerium 2-ethylhexanoate can provide an approximation of the decomposition temperatures and events of both precursor types. The main mass loss in the thermal decomposition of cerium acetate under an inert atmosphere (He) occurs in a temperature range between 200 and 500 °C.[59] In contrast, temperatures between 250 and 650 °C are required to cause the main mass loss in the thermal decomposition of cerium 2-ethylhexanoate.[60] Without generalizing, this example is useful to point out the expected requirement of higher temperatures to decompose 2-ethylhexanoate-based precursors when compared with acetate-based precursors. As the results suggest that the formation of La and Fe 2-ethylhexanoates proceeds at different rates and the formation of Co 2-ethylhexanoate was not identified, different ratios of (La, Fe, Co) precursors (acetates and 2-ethylhexanoates) are expected in the liquid phase (e.g., solutions and generated droplets). Together with the concentration variations, the differences in thermal decomposition of the acetate and 2-ethylhexanoate precursors would potentially cause the preferential decomposition of the acetate precursors leading to the mentioned nonhomogenous elemental distributions in the synthesized particles. Thus, the variation of the (La, Fe, Co) elemental distribution in the acetate-based samples can be related to the formation of the different identified RP, brownmillerite, and perovskite-type phases as found with the XRD analysis (Figure 3) and the associated diverse iron−oxygen coordination as identified in the Mössbauer analysis (Figure 6).

Contrary to the acetate-based cases, a high variation of the La, Fe, and Co elemental distributions in the small particles synthesized using nitrates as precursors was not identified (Figure 5). The liquid-phase FTIR results (Figure 9) hint only to a weak formation of iron 2-ethylhexanoate when nitrates are used as precursors, indicating a higher chemical stability (e.g., low degree of ligand-exchange reactions) of the nitrate-based solutions, which is most likely reflected in the high-elemental homogeneity of the produced small particles, having mainly the perovskite-type phase (Figure 3). Nevertheless, in the few encountered large particles (Figure 5), an enrichment of La and Fe is evident. The use of iron nitrate has been previously linked to the formation of large particles through the droplet-to-particle route in the spray-flame synthesis process, in which iron hydroxides, formed from the hydrolysis of iron in the liquid phase at low temperatures, precipitate to form such particles.[13] Furthermore, the content of iron nitrate in solutions of ethanol and 2-EHA has been related to the catalytic esterification of these solvents to form ethyl 2-ethylhexanoate and water, increasing the potential of the hydrolysis of iron and the formation of large particles.[13] This effect can be evidenced in the BET-specific surface area (SSA) results (Figure 2), in which the nitrate-based $x = 0.3$ sample presented a significantly lower SSA (61 m^2/g) than the $x = 0.2$ sample (100 m^2/g). When one assumes spherical and monodisperse particles, the lower SSA of the $x = 0.3$ sample is related to a higher number concentration and size of large particles.

3.3. Performance of the Materials in Oxygen Evolution Reaction (OER).

To analyze if the precursors used during the synthesis, in this case acetates and nitrates, influence the oxygen evolution reaction electrocatalytic activity of the resulted materials, RDE measurements were conducted and the recorded LSVs are presented in Figure 10.

Overall, the LSVs indicate a similar electrocatalytic activity for LaFe$_x$Co$_{1-x}$O$_3$ (x = 0.2, 0.3) obtained using the two different types of precursors. To reach a current density of 10 mA/cm^2, potentials around 1.6 V are required, with the acetate-based x = 0.2 requiring a slightly lower potential (~1.59(5) V), while for the x = 0.3, 20 mV higher potential was required. For the nitrate-based samples, the iron concentration does not influence the recorded current densities at all. Furthermore, lower slopes of the voltammograms in the linear region from 1.6 to 1.7 V are observed for the acetate-based samples in comparison with the nitrate-based

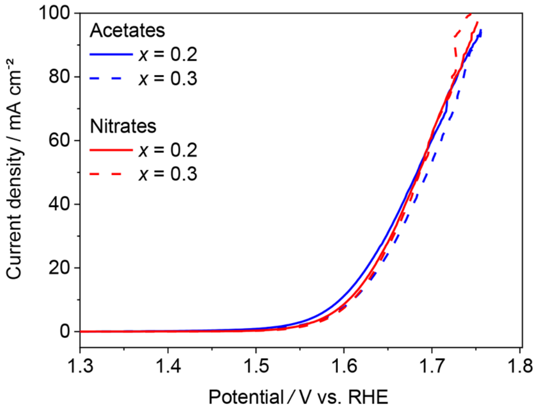

Figure 10. OER linear sweep voltammograms (LSV) of the acetate- and nitrate-based $LaFe_xCo_{1-x}O_3$ (x = 0.2, 0.3) samples with a scan rate of 5 mV/s and a rotation speed of 1600 rpm. Electrolyte: 1 mol/L KOH.

samples. This effect might be related to a lower electrical conductivity[61,62] of the oxygen-deficient structures, favored in the acetate-based samples in comparison with the oxygen-stoichiometric structures that are predominantly present in the nitrate-based samples.[63] The comparison of the $LaFe_xCo_{1-x}O_3$ (x = 0.2, 0.3) materials with similar compositions from the literature shows that the catalysts prepared in this study exhibit a medium-high electrocatalytic activity close to the state-of-the-art performance level (Table S4). Based on the findings of this study, an improvement of the homogeneity of La, Fe, and Co elemental distribution in the particles should be considered as a way to improve the activity of the catalysts. Additionally, better OER activities might be reached by further changing the Fe concentration (x) as it has been explored in the literature (Table S4). For example, targeting smaller step sizes (Δx), $LaFe_xCo_{1-x}O_3$ (x = 0−1, with Δx = 0.01 instead of Δx = 0.1), would help identify promising compositions. Nevertheless, this kind of mapping is time-consuming and challenging, making the use of high-throughput methods at different levels (synthesis, characterization, and electrochemical testing) mandatory. Furthermore, parameters related to the electrode preparation such as the Nafion-to-catalyst ratio, the type of substrate, or the coating technology can be explored to further improve the overall OER performance.

4. CONCLUSIONS

In this paper, we demonstrated that reactions in the precursor solution used for nanoparticle synthesis in spray flames influence the product composition and that the cations (nitrates vs acetates) affect the underlying reactions. Temperature-dependent ATR-FTIR measurements of the precursor solutions showed that, when metal acetates are used, ligand-exchange reactions lead to the preferential but incomplete formation of lanthanum and iron 2-ethylhexanoates. The practical consequence of this finding for the spray-flame synthesis is that, in the liquid phase, acetates and 2-ethylhexanoates coexist as precursors, and as these species have different decomposition temperatures, preferential decomposition of acetates over 2-ethylhexanoates is expected, thus influencing the product composition and structure and causing inhomogeneous La, Co, and Fe elemental distributions regardless of the size of the final particles. In contrast, when nitrates are used as precursors, the main effect observed is related to the esterification reaction of ethanol and 2-EHA to form 2-ethylhexanoate and water. The occurrence of water in the solution has been linked to hydrolysis reactions leading to the formation of metal hydroxides. This effect was found to be especially strong in the case of iron, causing precipitation of metal hydroxides in the precursor solution already at low temperatures leading to large particles. For materials synthesized from nitrates, inhomogeneous elemental distributions were encountered predominantly in the large particles.

For all samples, similar OER activities were identified, independent of the type of precursor used during the synthesis, requiring a potential of around 1.60 V vs RHE to reach a current density of 10 mA/cm^2. However, lower slopes of the voltammogram region from 1.6 to 1.7 V for the acetate-based samples hint to lower electrical conductivities of these samples in comparison to the nitrate-based samples.

■ ASSOCIATED CONTENT

Supporting Information

The Supporting Information is available free of charge at https://pubs.acs.org/doi/10.1021/acs.jpca.2c06601.

Fe 2p, Co 2p, C 1s, and La 3d X-ray photoelectron spectroscopy (XPS) spectra of acetate- and nitrate-based $LaFe_xCo_{1-x}O_3$ samples (x = 0.2 and 0.3), Rietveld refinements and FTIR measurements of as-synthesized and heat-treated samples, thermogravimetric analysis, inductively coupled plasma mass spectrometry (ICP-MS) measurements of the acetate- and nitrate-based $LaFe_{0.2}Co_{0.8}O_3$ samples, and comparison of the electrocatalytic activity of the samples prepared in this work and other similar reported samples for the oxygen evolution reaction (PDF)

■ AUTHOR INFORMATION

Corresponding Author

Steven Angel − *EMPI, Institute for Energy and Materials Processes − Reactive Fluids, University of Duisburg-Essen, 47048 Duisburg, Germany;* orcid.org/0000-0001-5390-2209; Email: steven.angel-canas@uni-due.de

Authors

Michael Braun − *Chemical Technology III, University of Duisburg-Essen, 47048 Duisburg, Germany*

Baris Alkan − *Fritz-Haber-Institut der Max-Planck Gesellschaft, Departments of Physical Chemistry and Inorganic Chemistry, 14195 Berlin, Germany*

Joachim Landers − *Experimental Physics, Faculty of Physics, University of Duisburg-Essen, 47048 Duisburg, Germany;* orcid.org/0000-0002-4506-6383

Soma Salamon − *Experimental Physics, Faculty of Physics, University of Duisburg-Essen, 47048 Duisburg, Germany;* orcid.org/0000-0002-8661-6038

Heiko Wende − *Experimental Physics, Faculty of Physics and CENIDE, Center for Nanointegration, University of Duisburg-Essen, 47048 Duisburg, Germany;* orcid.org/0000-0001-8395-3541

Corina Andronescu − *Chemical Technology III and CENIDE, Center for Nanointegration, University of Duisburg-Essen, 47048 Duisburg, Germany;* orcid.org/0000-0002-1227-1209

Christof Schulz − *EMPI, Institute for Energy and Materials Processes − Reactive Fluids and CENIDE, Center for*

Nanointegration, University of Duisburg-Essen, 47048 Duisburg, Germany; orcid.org/0000-0002-6879-4826

Hartmut Wiggers − *EMPI, Institute for Energy and Materials Processes − Reactive Fluids and CENIDE, Center for Nanointegration, University of Duisburg-Essen, 47048 Duisburg, Germany*

Complete contact information is available at: https://pubs.acs.org/10.1021/acs.jpca.2c06601

Notes

The authors declare no competing financial interest.

■ ACKNOWLEDGMENTS

The authors acknowledge funding by the German Research Foundation (DFG) within the SFB CRC/TRR 247 (project number 405366241 for subproject C02 and project number 388390466 for subproject B02) and by the Mercator Research Center Ruhr within the DIMENSION (Determining materials for energy conversion) project. XRD measurements from the group of Prof. Winterer (University of Duisburg-Essen) and ICP-MS measurements performed by Dr. Julia Büker and Jessica Aouag from the group of Prof. Muhler (Ruhr-University Bochum) are kindly acknowledged.

■ REFERENCES

(1) Albrecht, U.; Bünger, U.; Michalski, J.; Raksha, T.; Wurster, R.; Zerhusen, J. *International Hydrogen Strategies: A study commissioned by and in cooperation with the World Energy Council Germany*; Ludwig-Bölkow-Systemtechnik GmbH, Weltenergierat − Deutschland: Germany, 2020; p 167.

(2) Ede, S. R.; Luo, Z. Tuning the intrinsic catalytic activities of oxygen-evolution catalysts by doping: a comprehensive review. *Journal of Materials Chemistry A* **2021**, *9*, 20131−20163.

(3) Guo, Q.; Mao, J.; Huang, J.; Wang, Z.; Zhang, Y.; Hu, J.; Dong, J.; Sathasivam, S.; Zhao, Y.; Xing, G.; et al. Reducing Oxygen Evolution Reaction Overpotential in Cobalt-Based Electrocatalysts via Optimizing the "Microparticles-in-Spider Web" Electrode Configurations. *Small* **2020**, *16*, 1907029.

(4) Beall, C. E.; Fabbri, E.; Schmidt, T. J. Perovskite Oxide Based Electrodes for the Oxygen Reduction and Evolution Reactions: The Underlying Mechanism. *ACS Catal.* **2021**, *11*, 3094−3114.

(5) Granger, P.; Parvulescu, V.; Kaliaguine, S.; Prellier, W. *Perovskites and Related Mixed Oxides*; Wiley-VCH Verlag GmbH & Co. KGaA, 2016; p 1019.

(6) Fungerlings, A.; Koul, A.; Dreyer, M.; Rabe, A.; Morales, D. M.; Schuhmann, W.; Behrens, M.; Pentcheva, R. Synergistic Effects of Co and Fe on the Oxygen Evolution Reaction Activity of LaCo$_x$Fe$_{1\text{-}x}$O$_3$. *Chemistry* **2021**, *27*, 17145−17158.

(7) Brix, A. C.; Dreyer, M.; Koul, A.; Krebs, M.; Rabe, A.; Hagemann, U.; Varhade, S.; Andronescu, C.; Behrens, M.; Schuhmann, W. Structure-Performance Relationship of LaFe$_{1\text{-}x}$Co$_x$O$_3$ Electrocatalysts for Oxygen Evolution, Isopropanol Oxidation, and Glycerol Oxidation. *ChemElectroChem.* **2022**, *9*, e202200092.

(8) Angel, S.; Neises, J.; Dreyer, M.; Friedel Ortega, K.; Behrens, M.; Wang, Y.; Arandiyan, H.; Schulz, C.; Wiggers, H. Spray-flame synthesis of La(Fe, Co)O$_3$ nano-perovskites from metal nitrates. *AIChE J.* **2020**, *66*, e16748.

(9) Alkan, B.; Cychy, S.; Varhade, S.; Muhler, M.; Schulz, C.; Schuhmann, W.; Wiggers, H.; Andronescu, C. Spray-flame-synthesized LaCo$_{1\text{-}x}$Fe$_x$O$_3$ perovskite nanoparticles as electrocatalysts for water and ethanol oxidation. *ChemElectroChem.* **2019**, *6*, 4266−4274.

(10) Rosebrock, C. D.; Wriedt, T.; Mädler, L.; Wegner, K. The role of microexplosions in flame spray synthesis for homogeneous nanopowders from low-cost metal precursors. *AIChE J.* **2016**, *62*, 381−391.

(11) Jossen, R.; Pratsinis, S. E.; Stark, W. J.; Madler, L. Criteria for Flame-Spray Synthesis of Hollow, Shell-Like, or Inhomogeneous Oxides. *J. Am. Ceram. Soc.* **2005**, *88*, 1388−1393.

(12) Karaminejad, S.; Dupont, S. M. L.; Bieber, M.; Reddemann, M. A.; Kneer, R.; Dreier, T.; Endres, T.; Schulz, C. Characterization of spray parameters and flame stability in two modified nozzle configurations of the SpraySyn burner. *Proceedings of the Combustion Institute* **2022**; DOI: 10.1016/j.proci.2022.07.248.

(13) Angel, S.; Schneider, F.; Apazeller, S.; Kaziur-Cegla, W.; Schmidt, T. C.; Schulz, C.; Wiggers, H. Spray-flame synthesis of LaMO$_3$ (M = Mn, Fe, Co) perovskite nanomaterials: Effect of spray droplet size and esterification on particle size distribution. *Proceedings of the Combustion Institute* **2021**, *38*, 1279−1287.

(14) Alkan, B.; Medina, D.; Landers, J.; Heidelmann, M.; Hagemann, U.; Salamon, S.; Andronescu, C.; Wende, H.; Schulz, C.; Schuhmann, W.; et al. Spray-flame-prepared LaCo$_{1\text{-}x}$Fe$_x$O$_3$ perovskite nanoparticles as active OER catalysts: Influence of Fe content and low-temperature heating. *ChemElectroChem.* **2020**, *7*, 2564−2574.

(15) Chiarello, G. L.; Rossetti, I.; Forni, L.; Lopinto, P.; Migliavacca, G. Solvent nature effect in preparation of perovskites by flame-pyrolysis. *Applied Catalysis B: Environmental* **2007**, *72*, 218−226.

(16) Angel, S.; Tapia, J. D.; Gallego, J.; Hagemann, U.; Wiggers, H. Spray-Flame Synthesis of LaMnO$_{3+\delta}$ Nanoparticles for Selective CO Oxidation (SELOX). *Energy Fuels* **2021**, *35*, 4367−4376.

(17) Hardt, S.; Wlokas, I.; Schulz, C.; Wiggers, H. Impact of Ambient Pressure on Titania Nanoparticle Formation During Spray-Flame Synthesis. *J. Nanosci. Nanotechnol.* **2015**, *15*, 9449−56.

(18) Schulz, C.; Dreier, T.; Fikri, M.; Wiggers, H. Gas-phase synthesis of functional nanomaterials: Challenges to kinetics, diagnostics, and process development. *Proceedings of the Combustion Institute* **2019**, *37*, 83−108.

(19) An, S. R.; Song, K. H.; Lee, K. Y.; Park, K. T.; Jeong, S. K.; Kim, H. J. Fe-doped LaCoO$_3$ perovskite catalyst for NO oxidation in the post-treatment of marine diesel engine's exhaust emissions. *Korean Journal of Chemical Engineering* **2018**, *35*, 1807−1814.

(20) Kolotygin, V. A.; Viskup, A. P.; Pivak, E. V.; Kharton, V. V. The Mixed Electronic and Ionic Conductivity of Perovskite-Like Ba$_{1-x}$Sr$_x$Fe$_{1-y}$Ti$_y$O$_{3-\delta}$ and BaTi$_{0.5}$Fe$_{0.5-z}$Ce$_z$O$_{3-\delta}$ Solid Solutions. *Russian Journal of Electrochemistry* **2020**, *56*, 110−117.

(21) Russo, N.; Furfori, S.; Fino, D.; Saracco, G.; Specchia, V. Lanthanum cobaltite catalysts for diesel soot combustion. *Applied Catalysis B: Environmental* **2008**, *83*, 85−95.

(22) Durand, A. M.; Hamil, T. J.; Belanger, D. P.; Chi, S.; Ye, F.; Fernandez-Baca, J. A.; Abdollahian, Y.; Booth, C. H. The effects of Co$_3$O$_4$ on the structure and unusual magnetism of LaCoO$_3$. *J. Phys.: Condens. Matter* **2015**, *27*, 126001.

(23) Bill, E. ^{57}Fe-Mössbauer spectroscopy and basic interpretation of Mössbauer parameters. *Practical Approaches to Biological Inorganic Chemistry* **2020**, 201−228.

(24) Menil, F. Systematic trends of the ^{57}Fe Mössbauer isomer shifts in (FeO$_n$) and (FeF$_n$) polyhedra. Evidence of a new correlation between the isomer shift and the inductive effect of the competing bond T-X (→ Fe) (where X is O or F and T any element with a formal positive charge). *J. Phys. Chem. Solids* **1985**, *46*, 763−789.

(25) Kharton, V. V.; Patrakeev, M. V.; Tsipis, E. V.; Avdeev, M.; Naumovich, E. N.; Anikina, P. V.; Waerenborgh, J. C. Oxygen nonstoichiometry, chemical expansion, mixed conductivity, and anodic behavior of Mo-substituted Sr$_3$Fe$_2$O$_{7\text{-}\delta}$. *Solid State Ionics* **2010**, *181*, 1052−1063.

(26) Istomin, S. Y.; Tyablikov, O. A.; Kazakov, S. M.; Antipov, E. V.; Kurbakov, A. I.; Tsirlin, A. A.; Hollmann, N.; Chin, Y. Y.; Lin, H. J.; Chen, C. T.; et al. An unusual high-spin ground state of Co^{3+} in octahedral coordination in brownmillerite-type cobalt oxide. *Dalton Transactions* **2015**, *44*, 10708−13.

(27) Zhang, X.; Pei, C.; Chang, X.; Chen, S.; Liu, R.; Zhao, Z. J.; Mu, R.; Gong, J. FeO$_6$ Octahedral Distortion Activates Lattice Oxygen in Perovskite Ferrite for Methane Partial Oxidation Coupled with CO$_2$ Splitting. *J. Am. Chem. Soc.* **2020**, *142*, 11540−11549.

(28) Svensson, G.; Samain, L.; Biendicho, J.; Mahmoud, A.; Hermann, R.; Istomin, S.; Grins, J. Crystal Structure and Coordination of B-Cations in the Ruddlesden−Popper Phases $Sr_{3-x}Pr_x(Fe_{1.25}Ni_{0.75})O_{7-\delta}$ ($0 \leq x \leq 0.4$). *Inorganics* **2018**, *6*, 89.

(29) Murray-Rust, D. M.; Brewer Hartley, H. The dissociation of acids in methyl and in ethyl alcohol. *Proceedings of the Royal Society of London. Series A, Containing Papers of a Mathematical and Physical Character* **1929**, *126*, 84−106.

(30) Hueso, J.; Caballero, A.; Ocaña, M.; González-Elipe, A. Reactivity of lanthanum substituted cobaltites toward carbon particles. *J. Catal.* **2008**, *257*, 334−344.

(31) Wang, S.; Xu, X.; Zhu, J.; Tang, D.; Zhao, Z. Effect of preparation method on physicochemical properties and catalytic performances of $LaCoO_3$ perovskite for CO oxidation. *Journal of Rare Earths* **2019**, *37*, 970−977.

(32) Chiang, C. L.; Yang, J. M. Flame retardance and thermal stability of polymer/graphene nanosheet oxide composites. *Novel Fire Retardant Polymers and Composite Materials* **2017**, 295−312.

(33) Cheng, G.; Calizo, I.; Hacker, C. A.; Richter, C. A.; Hight Walker, A. R. Fe-catalyzed etching of exfoliated graphite through carbon hydrogenation. *Carbon N Y* **2016**, *96*, 311−315.

(34) Stoch, J.; Gablankowska-Kukucz, J. The effect of carbonate contaminations on the XPS O 1s band structure in metal oxides. *Surf. Interface Anal.* **1991**, *17*, 165−167.

(35) Li, J. P. H.; Zhou, X.; Pang, Y.; Zhu, L.; Vovk, E. I.; Cong, L.; van Bavel, A. P.; Li, S.; Yang, Y. Understanding of binding energy calibration in XPS of lanthanum oxide by in situ treatment. *Phys. Chem. Chem. Phys.* **2019**, *21*, 22351−22358.

(36) Armelao, L.; Bettinelli, M.; Bottaro, G.; Barreca, D.; Tondello, E. $LaCoO_3$ nanopowders by XPS. *Surface Science Spectra* **2001**, *8*, 24−31.

(37) Seiferth, O.; Wolter, K.; Dillmann, B.; Klivenyi, G.; Freund, H. J.; Scarano, D.; Zecchina, A. IR investigations of CO_2 adsorption on chromia surfaces: Cr_2O_3 (0001)/Cr(110) versus polycrystalline α-Cr_2O_3. *Surf. Sci.* **1999**, *421*, 176−190.

(38) Klingenberg, B.; Vannice, M. A. Influence of Pretreatment on Lanthanum Nitrate, Carbonate, and Oxide Powders. *Chem. Mater.* **1996**, *8*, 2755−2768.

(39) Tascón, J. M. D.; Tejuca, L. G. Adsorption of CO2 on the perovskite-type oxide LaCoO3. *Journal of the Chemical Society, Faraday Transactions 1: Physical Chemistry in Condensed Phases* **1981**, *77*, 591.

(40) Rosid, S. J. M.; Toemen, S.; Iqbal, M. M. A.; Bakar, W.; Mokhtar, W.; Aziz, M. M. A. Overview performance of lanthanide oxide catalysts in methanation reaction for natural gas production. *Environ. Sci. Pollut Res. Int.* **2019**, *26*, 36124−36140.

(41) Czylkowska, A.; Markiewicz, M. Synthesis, thermal behavior, and other properties of Y(III) and La(III) complexes with 4,4′-bipyridine and trichloro- or dibromoacetates. *J. Therm. Anal. Calorim.* **2012**, *109*, 727−734.

(42) Taguchi, Y.; Noguchi, T. Drastic changes in the ligand structure of the oxygen-evolving Mn cluster upon Ca^{2+} depletion as revealed by FTIR difference spectroscopy. *Biochim. Biophys. Acta* **2007**, *1767*, 535−40.

(43) Nelson, P. N.; Taylor, R. A. Theories and experimental investigations of the structural and thermotropic mesomorphic phase behaviors of metal carboxylates. *Applied Petrochemical Research* **2014**, *4*, 253−285.

(44) Sudheendra, L.; Motin Seikh, M.; Raju, A. R.; Narayana, C. An infrared spectroscopic study of the low-spin to intermediate-spin state ($^1A_1$−$^3T_1$) transition in rare earth cobaltates, $LnCoO_3$ (Ln = La, Pr and Nd). *Chem. Phys. Lett.* **2001**, *340*, 275−281.

(45) Haye, E.; Andre, E.; Capon, F.; Barrat, S.; De La Pierre, M.; Dovesi, R.; Carteret, C. Experimental and Theoretical Infrared Signatures of $REMO_3$ (RE = La, Pr, Nd, Sm, and M = Co, Fe) Perovskites. *J. Phys. Chem. C* **2018**, *122*, 10519−10525.

(46) Kim, I.; Choi, M. First-Principles Study of Anisotropic Oxygen Diffusion in $PrBaCo_2O_{5.5}$. *ACS Omega* **2019**, *4*, 10960−10964.

(47) Radaelli, P. G.; Cheong, S. W. Structural phenomena associated with the spin-state transition in $LaCoO_3$. *Physical Review B* **2002**, *66*, 094408.

(48) Patil, K. C.; Chandrashekhar, G. V.; George, M. V.; Rao, C. N. R. Infrared spectra and thermal decompositions of metal acetates and dicarboxylates. *Can. J. Chem.* **1968**, *46*, 257−265.

(49) Călinescu, M.; Negreanu-Pîrjol, T.; Georgescu, R.; Călinescu, O. Synthesis and characterization of new copper(II) complex compounds with chlorhexidine. Part I. *Open Chemistry* **2010**, *8*, 543−549.

(50) Zhu, H. J.; Hill, R. H. The photochemical metal organic deposition of manganese oxide films from films of manganese(II) 2-ethylhexanoate: a mechanistic study. *J. Non-Cryst. Solids* **2002**, *311*, 174−184.

(51) Palacios, E. G.; Juárez-López, G.; Monhemius, A. J. Infrared spectroscopy of metal carboxylates. *Hydrometallurgy* **2004**, *72*, 139−148.

(52) Mishra, S.; Daniele, S.; Hubert-Pfalzgraf, L. G. Metal 2-ethylhexanoates and related compounds as useful precursors in materials science. *Chem. Soc. Rev.* **2007**, *36*, 1770−1787.

(53) Bao, L.; Low, W.-L.; Jiang, J.; Ying, J. Y. Colloidal synthesis of magnetic nanorods with tunable aspect ratios. *J. Mater. Chem.* **2012**, *22*, 7117.

(54) Crabtree, R. H.; Rice, N. M. A spectrophotometric study of the organic phase complexes formed in the extraction of Cobalt II with carboxylic acids. In *International Solvent Extraction Conference ISEC'74* (Thornton, J. D., Naylor, A., McKay, H. A. C., Jeffreys, G. V., Eds.), Lyon, France, 1974; Vol. *I*, pp 791−822.

(55) Mowla, O.; Kennedy, E.; Stockenhuber, M. In-situ FTIR study on the mechanism of both steps of zeolite-catalysed hydroesterification reaction in the context of biodiesel manufacturing. *Fuel* **2018**, *232*, 12−26.

(56) Olewnik, E.; Nowaczyk, J.; Garman, K.; Czerwinski, W. Influence of ozone treatment on structure and thermal properties of bis-2-hydroxyethyl terephthalate-based copolymers. *J. Therm. Anal. Calorim.* **2013**, *112*, 697−702.

(57) Hienerwadel, R.; Boussac, A.; Breton, J.; Diner, B. A.; Berthomieu, C. Fourier transform infrared difference spectroscopy of photosystem II tyrosine D using site-directed mutagenesis and specific isotope labeling. *Biochemistry* **1997**, *36*, 14712−23.

(58) Shi, H.; Wang, Y.; Hua, R. Acid-catalyzed carboxylic acid esterification and ester hydrolysis mechanism: acylium ion as a sharing active intermediate via a spontaneous trimolecular reaction based on density functional theory calculation and supported by electrospray ionization-mass spectrometry. *Phys. Chem. Chem. Phys.* **2015**, *17*, 30279−91.

(59) Arii, T.; Taguchi, T.; Kishi, A.; Ogawa, M.; Sawada, Y. Thermal decomposition of cerium(III) acetate studied with sample-controlled thermogravimetric−mass spectrometry (SCTG—MS). *Journal of the European Ceramic Society* **2002**, *22*, 2283−2289.

(60) Morlens, S.; Ortega, L.; Rousseau, B.; Phok, S.; Deschanvre, J. L.; Chaudouet, P.; Odier, P. Use of cerium ethylhexanoate solutions for preparation of CeO2 buffer layers by spin coating. *Materials Science and Engineering: B* **2003**, *104*, 185−191.

(61) Kim, Y. T.; Lopes, P. P.; Park, S. A.; Lee, A. Y.; Lim, J.; Lee, H.; Back, S.; Jung, Y.; Danilovic, N.; Stamenkovic, V.; et al. Balancing activity, stability and conductivity of nanoporous core-shell iridium/iridium oxide oxygen evolution catalysts. *Nat. Commun.* **2017**, *8*, 1449.

(62) Luo, X. D.; Gao, R. L.; Fu, C. L.; Cai, W.; Chen, G.; Deng, X. L.; Zhang, H. R.; Sun, J. R. Resistance switching mechanism of $La_{0.8}Sr_{0.2}MnO_{3-\delta}$ thin films. *Physica B: Condensed Matter* **2016**, *483*, 99−102.

(63) Grunbaum, N.; Mogni, L.; Prado, F.; Caneiro, A. Phase equilibrium and electrical conductivity of $SrCo_{0.8}Fe_{0.2}O_{3-\delta}$. *J. Solid State Chem.* **2004**, *177*, 2350−2357.

https://doi.org/10.1021/acs.jpca.2c06601
J. Phys. Chem. A 2023, 127, 2564−2576